Numerical Simulation and Experimental Investigation into the Brittle Fracture Mechanism of 2195 Aluminum Alloy Ingot during Semi-Continuous Casting

Yuge Luo[1], Zihan Yang[1], Chen Shi[1], Jin Zhang[1], *Zhilin Liu[1]

1. Light Alloy Research Institute, Laboratory of Precision Manufacturing for Extreme Service Performance, Central South University, Changsha, 410083, China.

*Corresponding address: e-mail: zhilin.liu@csu.edu.cn

Abstract: During vertical semi-continuous casting processes, the thermal stress and corresponding strain generated in high-strength aluminum alloys may induce the formation of microcracks at different locations within the ingot. These microcracks originate from tensile thermal stress fields and propagate rapidly during subsequent cooling stages, ultimately leading to rejection of cast ingots through a phenomenon termed cold cracking. Numerical modeling enables simulation of the thermomechanical behavior of ingots during casting and post-solidification phases, thereby revealing critical cooling conditions responsible for catastrophic failure. In this study, fracture mechanics principles were initially employed to derive critical stress magnitudes for ingot failure, followed by residual thermal stress characterization in 2195 alloy ingot during semi-continuous casting using ProCAST software. Integration of mechanical analysis with simulation outcomes enabled determination of critical crack lengths in cast ingots. Results demonstrate a ductile-to-brittle transition occurring at a critical temperature of 200 ℃, with corresponding yield strength and elongation measuring 161.0 MPa and 3.3%, respectively. Circumferential compressive stresses dominate surface regions while tensile stresses concentrate centrally, establishing stress state conditions that promote straight-line cracking patterns in 2195 aluminum alloy ingots.

Keywords: Vertical semi-continuous casting; 2195 aluminum-lithium Alloy; Cold crack; Stress distribution; Mechanical properties.

1 Introduction

The semi-continuous casting process has been extensively implemented in large-scale aluminum alloy ingot production due to its efficiency advantages and process adaptability. However, residual thermal stresses generated during solidification and cooling phases readily induce crack defects, significantly compromising structural integrity and mechanical properties of cast products. The 2195 aluminum-lithium alloy, renowned for its high specific strength and widely applied in aerospace engineering, exhibits pronounced susceptibility to stress-induced cracking during casting processes. This phenomenon stems from lithium addition, which increases elastic modulus [1] while reducing thermal conductivity, thereby exacerbating thermal stress accumulation. Macro-defects formed on ingot surfaces provide nucleation sites for stress-concentrated thermal cracking. To effectively suppress ingot cracking, systematic optimization of critical process parameters is required, including alloy melt temperature, casting speed, cooling intensity, mold liquid level height, and flow stability, thereby enhancing surface quality and eliminating crack initiation sources. Specific control strategies encompass: (1) Synergistic optimization of process parameters (covering cooling water flow rate, purity, and spray pattern); (2) Rational regulation of pouring temperature (recommended maintenance at 10-20 ℃ above alloy liquidus temperature [2]) to prevent abrupt temperature gradient changes induced by melt superheat; (3) Implementation of scraper plate devices to interrupt water flow along ingot bottom; (4) Application of thermal insulation layers at ingot-mold interfaces to reduce interfacial heat transfer efficiency; (5) Strict control of impurity content (particularly sodium) through raw material purification (utilizing high-purity refined aluminum and lithium ingots) and optimization of primary alloy element ratios [3]. Elucidating the crack initiation and propagation mechanisms under complex thermo-mechanical coupling fields holds significant theoretical value for casting process optimization and product quality control. Current research demonstrates that directional microstructure optimization through semi-continuous casting parameter regulation can effectively enhance comprehensive alloy performance.

Existing research has systematically revealed the synergistic interaction mechanisms between residual stresses and material embrittlement effects on crack formation [4]. Lalpoor et al. [5] experimentally demonstrated through 7050 aluminum alloy studies that when material temperature decreases from 400 ℃ to 200 ℃, its plasticity index shows significant deterioration (impact toughness sharply declines from 10 J to 2 J). Numerical simulation technology has been successfully applied in predicting stress evolution during solidification processes. The ALSPEN model developed by Hallvard et al. [6] accurately simulated thermally induced stress/strain fields under water cooling conditions for 6063 aluminum alloy at a casting speed of 1.67 mm/s, revealing that viscoplastic strain in high-temperature ingot regions is dominated by creep mechanisms. Fjaer et al. [7] identified substantial axial viscoplastic strain in the solidification front region of ingots during semi-continuous casting through stress field simulations, with radial and circumferential components of stress tensor generating high tensile stresses during transverse contraction. Ludwig et al. [8] and Boender et al. [9] innovatively integrated the maximum principal stress criterion with fracture mechanics theory to establish quantitative assessment models for critical crack dimensions. Lalpoor et al. [10] elucidated cold cracking mechanisms in 7050 alloy through numerical stress field simulations, identifying accumulated tensile stresses during withdrawal as the primary cause of crack initiation, while surface compressive stress fields inhibit crack propagation. These findings provide valuable references for the current study, particularly in establishing critical crack size criteria and cold cracking evaluation frameworks. However, current research exhibits limitations in systematic integration of stress field simulation, fracture toughness assessment, and microstructural characterization, particularly regarding targeted investigations on 2195 Al-Li alloys. Previous studies predominantly focused on macroscopic stress distribution patterns, while insufficiently addressing the coupling mechanisms between local stress concentration effects, temperature-dependent material property variations, and microstructural characteristics (including grain boundary properties and interdendritic precipitate distributions). These knowledge gaps substantially impede accurate prediction of critical cracking thresholds and optimization of crack suppression strategies.

This study establishes an integrated research framework combining numerical modeling and experimental validation to systematically investigate the cracking behavior in 2195 Al-Li alloy during semi-continuous casting, developing a multi-scale correlation-based theoretical framework for casting crack prediction and suppression. The primary research objectives include: (1) Quantitative characterization of spatiotemporal evolution patterns of residual stresses (with emphasis on maximum principal stress component) in characteristic regions of ingots (surface zone, central zone, and mid-radius zone); (2) Evaluation of casting condition effects on temperature-dependent fracture toughness and establishment of failure criterion for critical crack size; (3) Revelation of structure-property relationships between microstructural characteristics and crack propagation paths, with clarification of dominant mechanisms governing cold cracking susceptibility. The findings provide scientific guidance for cooling rate regulation, process parameter optimization, and microstructural design, significantly enhancing casting reliability. Key results demonstrate that the ingot central zone sustains maximum tensile stress (94.6 MPa) at 200 seconds of solidification, corresponding to the brittle-ductile transition temperature range near 200 ℃. Under these thermal conditions, material fracture toughness exhibits abrupt reduction with critical crack size reaching minimum value (7.71 mm), substantially increasing catastrophic cracking risks. Although transient tensile stress peak (39.1 MPa) emerges in surface regions at 89 seconds of solidification, subsequent compressive stress fields effectively inhibit crack propagation. Microstructural analysis reveals preferential crack propagation along grain boundaries and interdendritic weak regions, while ductile matrix phases generate significant crack blunting effects. These discoveries confirm synergistic regulatory effects of macroscopic stress states and microstructural heterogeneity on cracking behavior.

2 Experimental procedure

A numerical simulation analysis of the temperature field and stress field for 2195 aluminum alloy round ingot was conducted using ProCAST software. The constructed geometric model comprised critical components including the hot top, mold, secondary cooling zone, and casting zone (Fig. 1). For the simulation of semi-continuous casting processes, the withdrawal speed was set to 35 mm/min, which represents the industrial standard for casting 2195 alloy (detailed process parameters are provided in Table 1). The casting process was simulated by moving the ingot bottom downward while maintaining fixed positions for the mold, hot top, and molten metal free surface. Time-dependent thermal boundary conditions were specifically defined to account for filling time, air gap formation between the ingot and bottom, air gap development on the ingot surface, as well as thermal conduction variations across different sections of the casting system.

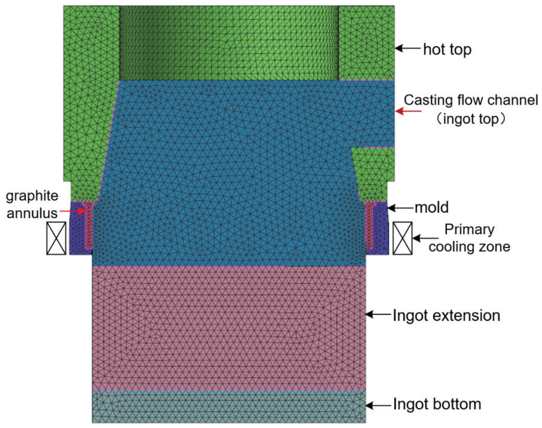

Fig. 1: The geometric configuration employed in the simulation of continuous casting ingot, depicting the hot top, mold, and cast alloy section

Table 1. Semi-Continuous Casting Process Parameters

Parameters	Details
Ingot diagram (mm)	405
Ingot length (mm)	2000
Casting speed (mm/min)	35
Casting temperature (℃)	695
Water follow rate (m^3/h)	12
Water temperature (℃)	25
withdrawal bottom initial temperature (℃)	25

The industrial production casting process was implemented based on the parameters specified in Table 1. The metallurgical system comprises: 1) A sealed top cover apparatus integrated with liquid level-temperature-pressure sensing systems; 2) An independently developed intelligent casting withdrawal mechanism featuring a programmable logic controller (PLC)-driven precision casting rate regulation system (maximum withdrawal speed of 100 mm • min^{-1}, displacement control accuracy of ± 0.01 mm); 3) A directional solidification mold with structural parameters of 405 mm inner diameter, 600 mm outer diameter, and 150 mm height. The communication architecture employs industrial bus technology for multi-parameter collaborative control. Analytical instrumentation includes a scanning electron microscope (SEM) (vision: TESCNA MIRA4) and a mechanical tensile testing machine (vision: CMT6130) coupled with a tubular resistance furnace (vision: YKRL-1200). The tensile mechanical properties of the as-cast 2195 alloy specimens were determined using the tensile testing method, with the results summarized in Table 2. The true stress-strain curves of radial specimens at a strain rate of 10^{-4} s^{-1} are presented in Fig. 2. The material exhibited increased brittleness and reduced ductility when temperatures fell below 400 ℃. Below 200 ℃, the alloy underwent brittle fracture with complete loss of ductility while maintaining elevated fracture strength. At ambient temperature, the yield (fracture) strength reached 232.7 MPa, which progressively declined to 55.6 MPa as temperature increased to 400 ℃. The temperature-dependent variations in yield strength and ductility (percentage elongation) are illustrated in Fig. 2 and Fig. 3. A similar behavior was observed: the yield strength demonstrated a linear enhancement with decreasing temperature as the material transitioned to a brittle state below 200 ℃, accompanied by a concurrent reduction in area values that followed an analogous trend.

Table 2. Mechanical properties of as-cast 2195 alloy obtained by tensile testing

Temperature (℃)	Yield strength (MPa)	Reduction of area (Pct)	Elongation (Pct)	Young modulus (MPa)
25	232.7	0.1	2.1	72359
100	205.0	0.5	2.8	73307
200	161.0	9.8	3.3	68311
300	98.5	36.6	5.2	54340
400	55.6	48.3	5.9	36938
500	22.4	60.0	6.6	16198
600	3.1	77.3	9.3	2428

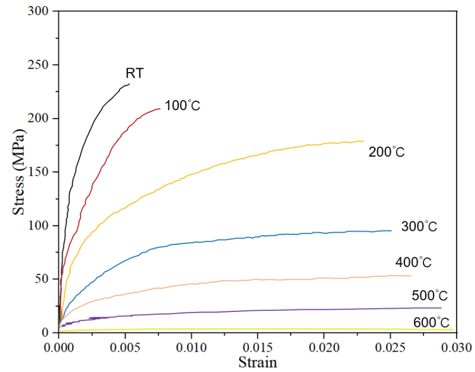

Fig. 2: the stress-strain testing curves of 2195 (radially sectioned) under varying temperatures at a strain rate of 10^{-4} s^{-1}

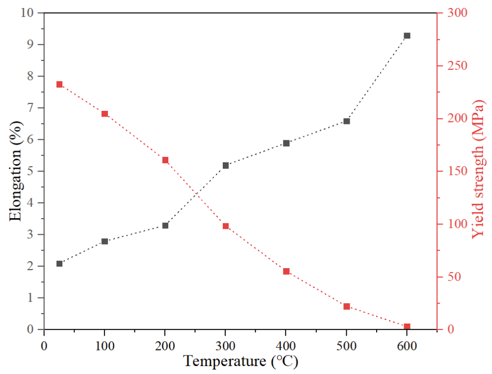

Fig. 3: Average elongation and average yield strength of 2195 (radially sectioned) at different temperatures

Fig. 4 illustrates the elongation curves along the ingot radius. It can be observed that the material exhibits pronounced brittle characteristics below 200 ℃, with an elongation rate of approximately 2%. In contrast, at 400 ℃, a significant divergence emerges in the elongation curve compared to that at 200 ℃, where the ductility at the ingot center reaches its maximum while surface ductility declines to its minimum. The research findings demonstrate a marked discrepancy in ductility between the central and peripheral regions at identical radial positions of the same casting, indicating significant heterogeneity in radial ductility within the ingot.

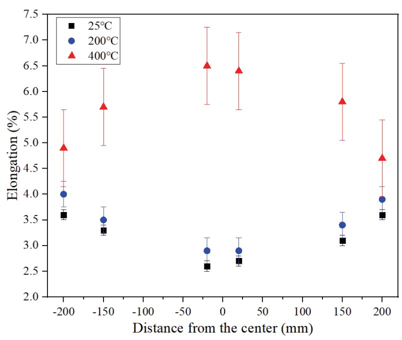

Fig. 3: The elongation of samples sectioned along the axial direction of the ingot at six distinct positions. The results illustrate variations under three different temperatures with a strain rate of 10^{-2} s^{-1}

To simulate the cooling process of the continuous casting ingot from the solidus temperature to room temperature, the extended Ludwik equation was employed in this study. This equation defines the stress σ as a function of ε_p, $\dot{\varepsilon}_p$, and T, with experimental curves fitted through the following formulation:

$$\sigma = K(T)\left(\varepsilon_p + \varepsilon_p^0\right)^{n(T)}\left(\dot{\varepsilon}_p\right)^{m(T)} \tag{1}$$

In the equation, $K(T)$ denotes the fracture toughness of the alloy, $n(T)$ denotes the strain hardening coefficient, $m(T)$ denotes the strain rate sensitivity, and ε_p^0 is a constant value of 0.001 [11]. This formulation is universally applicable to all aluminum alloys. The values of $K(T)$, $n(T)$, and $m(T)$ are incorporated into the model using the ALSPEN fitting function [12], where m, n, and K are nonlinear functions of temperature T, and the total viscoplastic strain is treated as a unified quantity. Notably, the conventional concept of "static yield stress" is absent in the mathematical description of viscoplastic strain. Within the material characterization framework, this study exclusively defines the flow stress σ, which depends on the effective viscoplastic strain rate and temperature. Consequently, any non-zero σ value theoretically induces viscoplastic strain at arbitrary temperatures. However, under low-temperature conditions ($<T_0$), σ diminishes significantly, causing the viscoplastic strain rate to asymptotically approach zero. Thus, viscoplastic strain becomes negligible at cryogenic temperatures.Additionally, this study introduces a hardening parameter that characterizes isotropic strain hardening of materials to approximate their strain behavior. In classical time-independent plasticity theory, the isotropic strain hardening effect is considered through the relationship between effective stress and incremental effective plastic strain. However, to account for the temperature and strain rate dependencies, the theory incorporates the effective viscoplastic strain rate, while introducing temperature T as an evaluation criterion in this relationship. Considering exclusively the strain hardening behavior at a specific reference temperature T_0 since all viscoplastic strains can be assumed to originate from creep above T_0 the aforementioned hardening parameter is defined as:

$$\alpha = \int d\alpha, \alpha = \begin{Bmatrix} d\bar{\varepsilon}_p, T \le T_0 \\ 0, T > T_0 \end{Bmatrix} \tag{2}$$

The initial temperature T_0 was determined as 200 ℃ based on stress-strain tests, above which strain hardening can be neglected (i.e., m=0). When the temperature exceeds T_0, the ALSPEN equation and cohesive model [13] were integrated for analysis, with Poisson's ratio values referenced from Table 3.

Table 3. The fracture toughness and Poisson's ratio derived from the constitutive parameter analysis of 2195 alloy

Temperature (℃)	fracture toughness (MPa)	*n*	*m*	Poisson's ratio
25	729.2	0.45	0	0.365
100	641.1	0.38	0	0.368
200	457.6	0.27	0	0.372
300	200.8	0.16	0.04	0.378
400	147.4	0.07	0.09	0.383
500	40.1	0.02	0.14	0.386
600	19.6	0.01	0.19	0.394

3 Results and discussion

3.1 Simulation Results

Given that the cold crack phenomenon occurs under fully solid-state material conditions, this investigation must not only examine the stress distribution under steady-state conditions but also conduct further analysis of stress states in the casting during the casting process and after water flow cessation. To achieve these objectives, the simulation experiment will be implemented according to the following protocol: The total experimental duration is 3800 seconds, comprising 1800 seconds of casting operation, followed by a gradual reduction of casting speed to zero from 1801 to 1900 seconds. The water flow in the cooling sidewalls is terminated at 2200 seconds, with subsequent air cooling maintained from 2201 to 3800 seconds. Notably, the entire ingot temperature remains within the range of 30-60 ℃ during this phase. As the current casting has already achieved steady-state conditions through 200 seconds of casting simulation, the 1800 s casting duration proves sufficient for comprehensive investigation of residual thermal stress evolution accumulated during the casting process. Fig. 5(a)-(d) present contour distribution diagrams of the four components of residual thermal stress in the continuously cast ingot after 3800 s of simulation. Following the cessation of casting and cooling water flow, the magnitude and distribution of stresses remained largely stable except in the upper mold contact zone and water impingement regions. Both transient and steady-state conditions demonstrated stabilized stress states when the lower ingot temperature decreased below 80 ℃. The contour plots reveal distinct spatial variations in thermal stress components: Radial residual stress exhibited tensile behavior at the ingot bottom, progressively diminishing toward the upper hot top end (Fig. 5a). Along the radial axis, the radial thermal stress decreased from maximum tensile stress (72 MPa) to near-0 values. Circumferential stress components followed comparable trends but transitioned to compressive stresses (-60 MPa) at the ingot periphery after reaching zero at intermediate radial positions (Fig. 5b). Axial thermal stress distribution mirrored this pattern in the lower ingot but diverged in upper regions, displaying tensile stresses below the mushy zone and compressive stresses near water impingement areas (Fig. 5c). Shear stress components predominantly manifested negative values, with maximum magnitudes occurring near secondary cooling water impact zones and the ingot base (Fig. 5d). Comprehensive analysis indicates that direct secondary cooling water impingement below the mold significantly influences the final stress state, particularly affecting circumferential components. Radial stress demonstrated maximum tensile values at the ingot centerline (lower section), decreasing radially toward the surface. Circumferential stresses transitioned from surface compression to central tension, with a neutral point at approximately half-radius (1/2 r). Shear stresses remained relatively minor except in localized regions adjacent to cooling water impact zones and the ingot base.

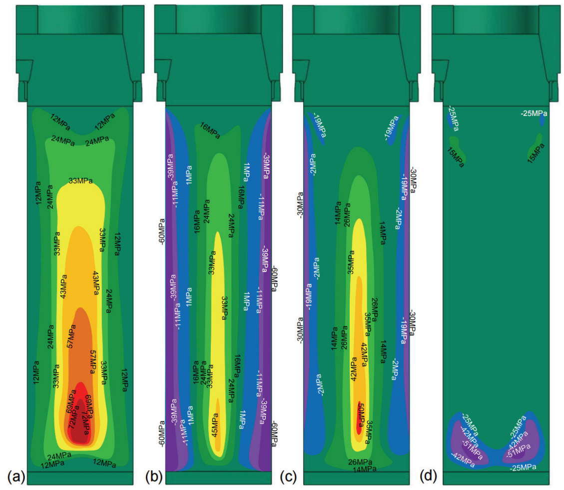

Fig. 5: Residual thermal stress from numerical simulation after 3800 s: (a) Radial; (b) Circumferential; (c) Axial; (d) Shear component

Fig. 6(a)-(d) present the contour distributions of the viscoplastic components. The radial strain component (Fig. 6a) exhibits tensile dominance in the middle-lower region of the ingot, with a reduction trend observed in the mid-radius zone. This tensile state subsequently intensifies again during radial movement toward the ingot surface. In the upper region of the casting, the plastic strain maintains relatively uniform and low levels except at the surface. Fig. 6b illustrates the circumferential strain component, showing tensile behavior in the central-bottom area of the ingot. This transitions to compressive strain during radial movement toward the surface, reaching maximum compression at the sub-surface layer of the ingot bottom. Distinct from radial and circumferential distributions, the axial component of plastic strain tensor (Fig. 6c) demonstrates negative values (compressive state) in the central region, gradually diminishing to zero toward the upper ingot. Conversely, the axial component displays mild tensile strain in surface regions, with minimum tensile values at the top and maximum tensile values at the bottom. The shear strain component (Fig. 6d) remains relatively small, achieving its maximum negative value in the lower ingot region adjacent to the bottom block.

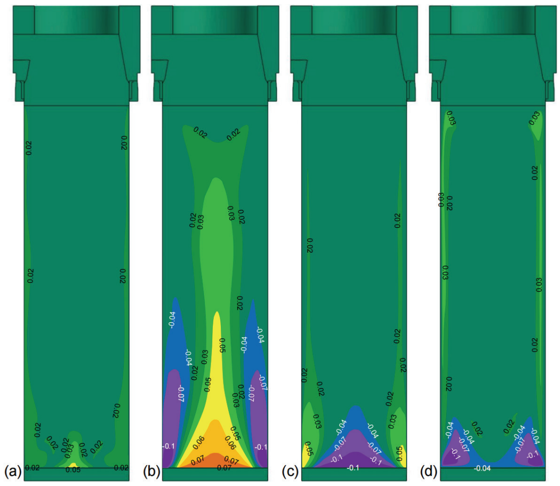

Fig. 6: Residual viscoplastic strain components from numerical simulation after 2800 s: (a) Radial; (b) Circumferential; (c) Axial; (d) Shear

To investigate the plastic yielding behavior of the ingot, contour maps of the hardening parameter, effective stress, and cumulative effective strain were plotted (Fig. 7a to 7c). In regions where the ingot temperature exceeded T_0 or exhibited no yielding (α=0), the total viscoplastic strain predominantly originated from creep mechanisms (Fig. 7a). The contour maps of effective stress and hardening parameter provide references for material yielding simulation results. As shown in Fig. 7b, the surface effective stress approached 100 MPa, significantly exceeding the residual deformation yield strength of 2195 aluminum alloy above 200 ℃. Two factors contributed to such high effective stress at the ingot surface: direct water flow impact generating high tensile stress, and substantial compressive accumulation in the lower ingot region (circumferential direction). Following pouring completion, the high tensile state induced by water flow impact diminished, transforming the surface stress state into high compression and causing localized plastic deformation. However, this deformation remained relatively limited, with maximum effective viscoplastic strain values of 0.012-0.014 concentrated near the surface layer and bottom centerline (Fig. 7c). The maximum principal stress component, whose contour map is presented in Fig. 7d, serves as an indicator for evaluating crack-prone zones. The maximum values emerged in the mid-lower ingot region (approximately 200 ℃ after 200 s of casting), where temperature conditions favored stress concentration. A detailed discussion of the maximum principal stress component's influence on cracking susceptibility will be addressed in the subsequent section.

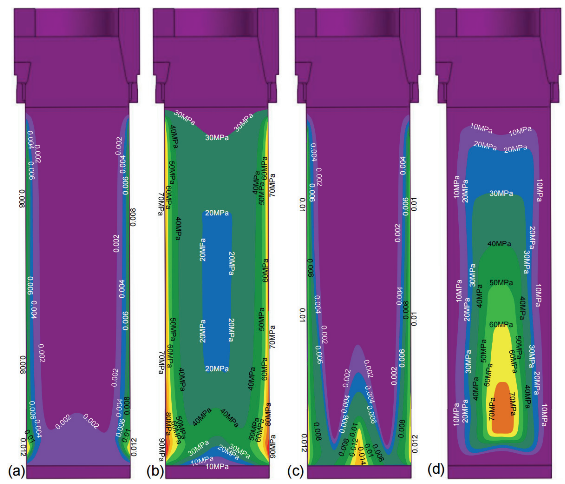

Fig. 7: Plastic yielding and strain hardening through contour maps derived from numerical simulations: (a) Hardening parameter; (b) Effective stress; (c) Cumulative effective strain; (d) Maximum component of principal stress.

3.2 Evaluation of Cracking

Assuming the maximum component of principal stress acts on the crack plane and considering the ingot as a semi-infinite medium, the maximum principal stress component can be utilized to evaluate cracking probability [14]. Prior to discussing this aspect, it is essential to investigate the evolution of the maximum principal stress component during the casting process. With the coordinate origin established at the bottom surface center of the ingot (x: 0 mm, y: 0 mm), stress analysis was conducted at the following critical locations: surface region (x: 200 mm, y: 60 mm), 1/2 r position (x: 100 mm, y: 60 mm), geometric center (x: 0 mm, y: 60 mm), and center+70 (x: 0 mm, y: 130 mm). The center+70 designation refers to the specific point exhibiting the peak maximum principal stress value within the ingot. Fig. 8 illustrates the temporal evolution of maximum principal stress components at these selected locations. The surface region demonstrates a stress peak of 39.1 MPa at 89 s of simulation time. Subsequent stress reduction in the surface layer primarily results from the transition in stress regime from tensile to compressive at the surface.

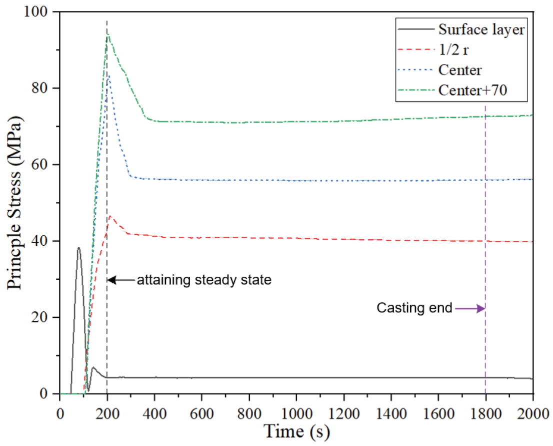

Fig. 8: The evolution of principal stress maxima (calculated simulation results) at four characteristic locations: Center (x: 0 mm, y: 60 mm), Center+70 (x: 0 mm, y: 130 mm), 1/2 r (x: 100 mm, y: 60 mm), and Surface layer (x: 200 mm, y: 60 mm)

On the other hand, as illustrated in Fig. 8, the principal stress at the ingot center reached its peak value of 94.6 MPa around 200 s. After attaining steady state, this stress value remained essentially constant even following the cessation of casting and shutdown of cooling water supply. However, it is noteworthy that under steady state conditions, the maximum principal stress component at the central location exhibited a slight upward trend, whereas the maximum principal stress component at the 1/2 r position demonstrated a gradual downward tendency. This phenomenon can be attributed to the progressive concentration of internal stresses toward the central axis over time. Furthermore, Fig. 8 distinctly reveals that the principal stress attained its maximum value more rapidly at the ingot surface, albeit with relatively lower stress magnitudes compared to internal regions.

At 200 s, the maximum principal stress component reaches its peak value at the center, thus enabling the evaluation of cracking probability based on the K_{Ic} value at this temperature. This study conducted plane strain fracture toughness tests across a temperature range from room temperature to 200 ℃. Metallic specimens with dimensions illustrated in Fig. 9(a) were polished to facilitate tracking and precise measurement of fatigue crack lengths. Specimens were subsequently fatigue pre-cracked at room temperature under a loading rate that maintained stress intensity at approximately 1.5 $MPa \cdot m^{1/2} \cdot s^{-1}$. For elevated temperatures, specimens were equilibrated in a muffle furnace for 20 minutes at target temperatures. K_{Ic} values from room temperature to 200 ℃ were calculated using load-displacement curves, as shown in Fig. 9(b). It can be observed that K_{Ic} exhibits a slight decrease with increasing temperature. Above 200 ℃, plane strain conditions become invalid, primarily attributable to a sudden decrease in yield strength (161.0 MPa at 200 ℃ versus 98.5 MPa at 300 ℃).

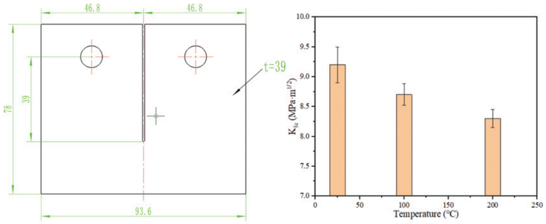

Fig. 9: the plane strain fracture toughness (KIc) values of the as-cast 2195 alloy: (a) Design size; (b) the temperature range from room temperature to 200 ℃

Considering that in casting practices, cracks with diverse geometric shapes may form central region, particularly in the ingot center and mid-radius area where penny-shaped cracks (PSC) of specific dimensions are highly probable. Based on the analysis by Griffith [15], the critical crack size corresponding to brittle fracture for this geometry is calculated as follows:

$$a_c = \frac{\pi}{4}\left(\frac{K_{Ic}}{\sigma}\right)^2 \qquad (3)$$

On the surface of ingot, whose critical crack size relates to K_{Ic} and stress through the following relationship [16]:

$$a_c = \frac{\pi}{(2\times 1.21)^2}\left(\frac{K_{Ic}}{\sigma}\right)^2 \qquad (4)$$

The critical crack sizes leading to catastrophic failure are illustrated in Fig. 11, located at the ingot center, center+70, 1/2 r, and surface layer. As the K_{Ic} value could only be measured at 200 ℃ and below, the critical crack sizes were calculated when the ingot temperature fell beneath this threshold. The critical crack size was determined using the aforementioned equation, correlating with principal stress values at these positions in the ingot (Fig. 7) and K_{Ic} (Table 3). Fig. 10 demonstrates that for PSC, the minimum critical crack sizes causing catastrophic failure at 200 ℃ occurred at the center, center+70, and 1/2 r positions, primarily attributed to the peak principal stress values at these locations. Below 200 ℃, a slight reduction in principal stress values resulted in increased critical crack sizes at these positions. Crack initiation probability also escalated when moving from the mid-radius toward the center. The maximum probability zone initiated approximately 70 mm above the bottom in the positive y-direction (orange region in Fig. 7d). The minimal critical crack size (7.71 mm) observed at 200 ℃ predominantly resulted from the maximum principal stress component reaching its peak value at this temperature.

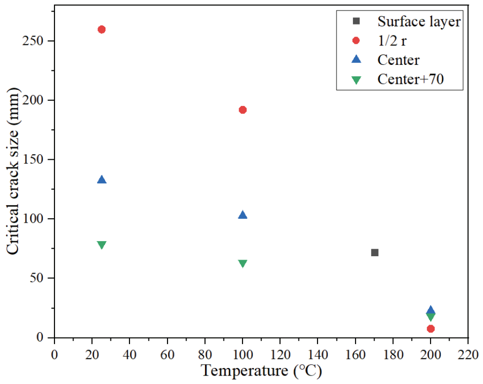

Fig. 10: the critical crack dimensions at the center, center+70, 1/2 r, and surface PSC locations of the ingot.

The maximum principal stress was observed at the slab surface within the water impingement zone when the temperature reached approximately 174 ℃ during an 80 s cooling process. Under these specific thermal-stress conditions, the critical crack size was calculated to be 72 mm (Fig. 10). During the casting process, surface stresses progressively transition to compressive stresses with increasing distance from the water impingement zone, as evidenced by the principal stress components exhibiting negative values at their maximum magnitudes.

3.3 Mechanistic Analysis

Based on the previously elucidated evolution patterns of residual thermal stress in semi-continuously cast cylindrical ingot, this study reveals that except for the initial stage where the ingot surface exhibits slight compressive stress due to contraction, the central region predominantly maintains tensile stress throughout the casting cycle. Concurrently, the surface stress manifests as tensile in the water impact zone but transitions to compressive during subsequent cooling. Consequently, two critical phases can be identified during semi-continuous casting of aluminum alloy ingot with specific dimensions: the first phase features high tensile stress formation at the surface after 80 seconds, while the second phase witnesses peak principal stress at the ingot center around 200 seconds. The initial high tensile stress at the surface may induce crack initiation, though subsequent compressive stress might close these surface cracks. However, during the transient tensile stress period, insufficient time exists for crack propagation to significant lengths. A more substantial risk emerges post-200 ℃ when material ductility diminishes and brittleness develops (as shown in Table 2), conditions favoring either new crack formation or propagation of existing cracks to critical PSC lengths (7.71-22.87 mm). In the ingot center, initial crack nucleation likely originates from hot tearing above solidus temperature, with subsequent propagation under radial, circumferential, or axial tensile stresses until reaching critical dimensions, ultimately predisposing the material to central cracking. Fig. 11 demonstrates a typical longitudinal penetrating crack failure in 2195 aluminum alloy semi-continuously cast ingot. The linear splitting pattern observed in the ingot cross-section (Fig. 11b) primarily results from combined circumferential and radial effects of the stress tensor (Fig. 5a and 5b). Notably, Fig. 11(c) illustrates how surface-proximate cracks closed and ceased propagation. This termination occurs through elastic energy release during crack propagation under tensile stress, coupled with protective compressive circumferential stress components at the surface (Fig. 7b) that effectively arrest further crack advancement.

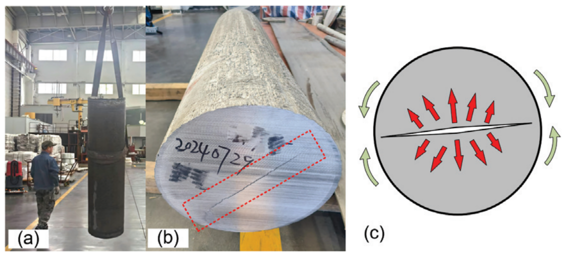

Fig. 11: A penetrating crack in a 405 mm-diameter 2195 aluminum alloy semi-continuous casting ingot: (a) product ingot casting; (b) Cross-sectional view of the crack; (c) Arrows indicate that compressive circumferential stress tends to arrest crack propagation

Fig. 12 displays the crack propagation morphology in the fracture cross-section sample captured via SEM, wherein cracks predominantly propagate along grain boundaries and interdendritic spaces. This phenomenon represents a typical manifestation of brittle intermetallic compounds (non-equilibrium eutectic phases)/ transgranular fracture modes [17]. These regions, influenced by the low-temperature mechanical properties of the alloy, are prone to intergranular fractures characterized by secondary cracks, pores, or crevices, rendering them the most susceptible sites for cold cracking. Consequently, they follow river-like propagation patterns [18] and may ultimately fail to align perpendicularly with the maximum principal stress component. Cracks may even arrest at the matrix (Fig. 12c and d), where sufficient plasticity exists to impede brittle fracture (Fig. 13). Therefore, the final morphology and microstructural characteristics of microcracks constitute the primary factors rendering cold cracking an unpredictable phenomenon. Practically, the triaxial stress state within the ingot combined with propagation pathways along grain boundaries and interdendritic spaces may promote microcrack formation, ultimately preventing their complete alignment with the normal direction of maximum principal stress or attainment of critical lengths for catastrophic propagation [19], thereby precluding cold cracking occurrence under such conditions [20].

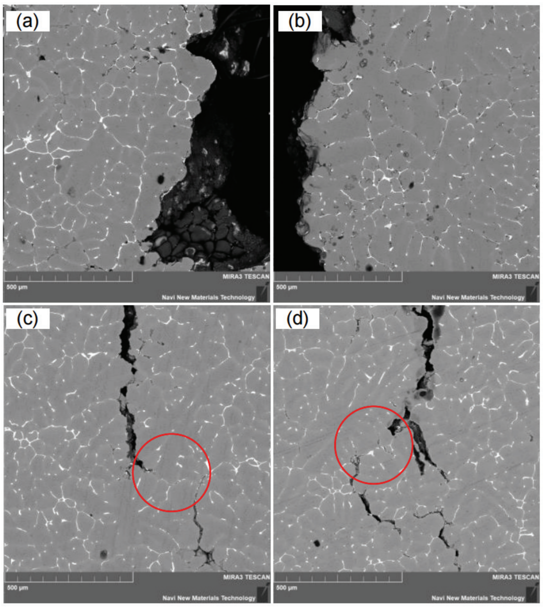

Fig. 12: SEM images of the propagation of microcracks: (a) Crack in the central region of the ingot (left-side matrix); (b) Crack in the central region of the ingot (right-side matrix); (c) One extremity of the crack; (d) The opposing extremity of the crack. (Red circles denote the interruption of crack progression upon reaching the matrix boundary)

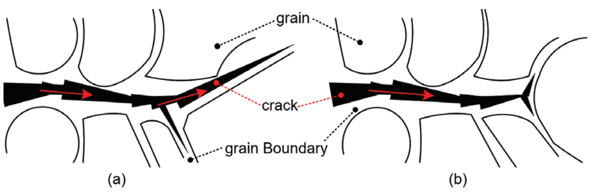

Fig. 13: Schematic illustration of crack propagation and arrest mechanisms: (a) Alteration in crack propagation direction due to grain boundary positioning; (b) Cessation of crack extension induced by obstruction from the matrix ahead of the crack front

4 Conclusions

This study investigates the stress field of 2195 aluminum alloy round ingot during semi-continuous casting through numerical simulation and experimental characterization, with particular emphasis on mechanical properties, fracture toughness, and cracking behavior. The principal findings are summarized as follows:

(1) A comprehensive simulation of stress distribution in 2195 alloy ingots was conducted using ProCast software, incorporating process parameters including withdrawal speed (35 mm/min) and cooling water flow rate (12 m^3/h), along with time-dependent thermal boundary conditions. Tensile testing revealed temperature-dependent mechanical properties: the material transitions to brittle behavior below 200 ℃, with yield strength inversely related to temperature (161.0 MPa at 200 ℃) and corresponding elongation of 3.3%.

(2) Simulation results demonstrate that residual radial stress at the ingot bottom exhibits tensile characteristics, peaking at the central region (72 MPa) and diminishing towards the surface. Circumferential stress manifests as compressive stress (-60 MPa) at the surface, while axial stress remains compressive at the center. Maximum shear stress occurs near the water impingement zone.

(3) Principal stress analysis indicates maximum central stress (94.6 MPa) occurs at approximately 200 seconds. Surface principal stress reaches peak value (39.1 MPa) at 89 seconds before declining due to stress state transformation. Critical crack size calculations identify minimum crack tolerance (7.71 mm) at the central region under 200 ℃ conditions, indicating highest fracture susceptibility.

(4) Surface tensile stress concentration in water impact zones promotes crack initiation, though subsequent compressive stress may induce crack closure. Conversely, central regions exhibit reduced ductility at 200 ℃, facilitating crack propagation to critical dimensions. Microscopic analysis reveals intergranular and interdendritic crack propagation, with final crack morphology and trajectory influenced by triaxial stress states and microstructural characteristics, contributing to unpredictable cold cracking behavior.

This integrated simulation-experimental approach elucidates the formation mechanism of residual stresses and crack initiation/propagation in 2195 aluminum alloy during semi-continuous casting. The study identifies high principal stresses in central regions combined with material embrittlement as primary contributors to cracking. Furthermore, triaxial stress states and microstructural-dependent crack propagation paths significantly influence cold cracking phenomena. These findings provide theoretical guidance for process optimization and crack mitigation in the aluminum alloy casting operations.

Acknowledgments

This research wasalso supported by the Natural Science Foundation of Hunan Province through Grant No. 2022JJ20066 (Excellent Youth Foundation) and the National Natural Science Foundation of China through Grant No. 5247053998.

Conflicts of interest:

The authors declare that they have no known competing financial interests or personal relationships that could have appeared to influence the work reported in this paper.

References

[1] Xue C, Zhang Y, Wang S, et al. Achieving highest Young's modulus in Al-Li by tracing the size and bonding evolution of Li-rich precipitates. J. Journal of Materials Science & Technology, 2023, 145: 125-135, https://doi: 10.1016/j.jmst.2022.10.052

[2] Wang T, Liang C, Chen Z, et al. Development of an 8090/3003 bimetal slab using a modified direct-chill casting process. J. Journal of Materials Processing Technology,2014,214(9):1806-1811.https://doi:10.1016/j.jmatprotec.2014.03.029

[3] Hongkai Z. Development of Production Technology of Aluminum-Lithium Alloys. J. Value in Health, 2012, 15(4):A128-A129.https://doi:10.1016/j.jval.2012.03.694.

[4] E. Niyama. Japan-USA Joint Seminar on Solidification of Metals and Alloys. J. National Science Foundation, 1977: 271-82.

[5] Lalpoor M, Eskin D G, Katgerman L. Fracture behavior and mechanical properties of high strength aluminum alloys in the as-cast condition. J. Materials Science & Engineering A, 2008, 497(1-2): 186-194. https://doi:10.1016/j.msea.2008.06.047

[6] Fjaer H G, Mo A. ALSPEN: a mathematical model for thermal stresses in direct chill casting of aluminium billets. J. Modeling, Identification and Control (MIC), 1993, 14(4). https://doi:10.4173/mic.1993.4.2.

[7] Chang K M, Lu H M, Wan J. 2nd Int. Conf. on Quenching and Control of Diffusion. ASM INTERNATIONAL. Materials Park, 1996: 341-45.

[8] Rappaz M, Ozgu M, Mahin K. Modeling of casting, welding and advanced solidification processes. J. Tms Publ, 1991. http://dx.doi.org

[9] Boender W, Burghardt A. Proc. 5th Decennial Int. Conf. On Solidification Processing. University of Sheffield. Sheffield. United Kingdom, 2007: 714-18.

[10] Lalpoor M, Eskin D G, Katgerman L. Cold-cracking assessment in AA7050 billets during direct-chill casting by thermomechanical simulation of residual thermal stresses and application of fracture mechanics. J. Metallurgical & Materials Transactions A, 2009, 40(13): 3304. https://doi:10.1007/s11661-009-0031-y.

[11] Magnin B, Katgerman L, Hannart B. Modeling of casting, welding and solidification process.MCWASP VII, M. Cross and J. Cambell, eds., TMS, Warrendale, PA. 1995: 303-10.

[12] Fjaer H G, Mo A. Metall. Trans. B, 1990, 21B: 1049-61.

[13] Martin C L, Ludwig O, Suery M. Mater. Sci. Forum, 2002, 396-402: 265-70.

[14] Boender W, Burghardt A, Klaveren E P V, et al. Numerical simulation of DC casting; Interpreting the results of a thermo-mechanical model. J. Tms Light Metals,2013,3:679-684.https://doi:10.1007/978-3-319-48228-6_118

[15] Carretero J A, Podhorodeski R P, Nahon M A, et al. Kinematic analysis and optimization of a new three degree-of-freedom spatial parallel manipulator. J. Journal of Mechanical Design, 2000, 122(1): 17-24. https://doi:10.1115/1.533542

[16] Rooke D P, Cartwright D J. Compendium of Stress Intensity Factors. J. H.M.S.O, 1976.

[17] Hess J B: Metall. Trans. A, 1983, 14A: 323-27.

[18] M'Hamdi M, Benum S, Mortensen D, et al. The importance of viscoplastic strain rate in the formation of center cracks during the start-up phase of direct-chill cast aluminum extrusion ingots. J. Metallurgical and Materials Transactions A, 2003. https://doi:10.1007/s11661-003-0159-0

[19] Lalpoor M, Eskin D G, Katgerman L. Numerical simulation of residual thermal stresses in AA7050 alloy during DC-casting using ALSIM5. J. Advanced Materials Research,2010,89-91:319-324. https://doi:10.4028/www.scientific.net/AMR.89-91.319.

[20] Caron E, Wells M A. Secondary cooling in the direct-chill casting of magnesium alloy AZ31. J. Metallurgical & Materials Transactions B, 2009, 40(4): 585-595. https://doi:10.1007/s11663-009-9254-y.